Quantifying the Effect of Nanofeature Size on the Electrical Performance of Black Silicon Emitter by Nanoscale Modeling

Shaozhou Wang, Giuseppe Scardera, Fa-Jun Ma, Yu Zhang, David Payne, Malcolm Abbott, and Bram Hoex

***Abstract*—Nanostructured black silicon (b-Si) surfaces with an extremely low reflectance are a promising light-trapping solution for silicon solar cells. However, it is challenging to develop a high-efficiency front-junction b-Si solar cell due to the inferior electrical performance of b-Si emitters, which outweighs any optical gain. This article uses three-dimensional numerical nanoscale simulations, which are corroborated with experiment results, to investigate the effect of the surface nanofeature sizes on the b-Si emitter performance in terms of the sheet resistance (R_{sheet}) and the saturation current density (J_{0e}). We show that the specific surface area (SSA) is an effective parameter to evaluate the nanofeature size. A shallow surface nanofeature with a large SSA will contribute to a better electrical performance. We will show that b-Si emitter R_{sheet} measured by a four-point probe is not a measure of the doping level in the nanofeature, but is ruled by the doping level in the underlying substrate region. We also show that a small nanofeature with SSA $> 100\ \mu m^{-1}$ and height < 100 nm can lead to a relatively low J_{0e} (33 fA/cm^2 lower than the best b-Si results reported in the literature) by suppressing surface minority carrier density and minimizing the total Auger recombination loss.**

***Index Terms*—Black silicon, numerical simulation, phosphorus diffusion, recombination loss, sheet resistance.**

I. INTRODUCTION

BLACK silicon (b-Si) generally refers to a type of low-reflectance silicon surface nanotexture that appears black to the naked eye. Depending on the preparation methods, these structured silicon surfaces have various nanoscale or microscale surface morphologies, such as cones, needles, columns, and holes [1]. Due to the excellent light management of the surface structured features, b-Si surfaces can achieve an extremely high photon absorption and, thus, are promising for a range of applications, such as photodetection[2], [3], gas sensing [4], mass spectrometry[5], and photo-electrocatalysis [6]–[9]. B-Si also shows great potential in solar cell applications, as was demonstrated for interdigitated-back-contact solar cells with an undiffused low-reflectance b-Si front surface [10]–[12]. This application benefits from the atomic-layer-deposited conformal thin films, which overcome b-Si surface passivation challenges [13]–[16]. Moreover, it has been found that there will be an effective reduction of surface recombination loss due to the enhanced field-effect for undiffused b-Si surfaces passivated with charged thin films [13], [17], [18]. However, for applying the low-reflectance b-Si on front-junction solar cells, there are no reported efficiencies higher than 20%. This is attributed to the inferior electrical performance which outweighs the gain in optical performance [19], [20].

Several attempts have been made to understand and optimize b-Si emitters in order to improve their electrical performance. Zhong *et al.* [20] reviewed the empirical investigations for suppressing the recombination losses in b-Si emitters and concluded that the root causes of the inferior electrical performance were the high surface recombination loss due to the enlarged surface area and also the severe emitter Auger recombination loss caused by the increased emitter volume with a higher post-diffusion doping level. As this problematic enhanced diffusion is also attributed to the enlarged surface area, one of the widely used optimization methods is reducing the heights of the surface nanofeatures and thus decreasing the surface area [21], [22]. Moreover, the surface morphology optimization can make b-Si emitters achieve comparable or even better electrical performance than the conventional microtextures [23]–[25], even though sacrificing some optical gains. However, how the nanofeature size affects the dopant distribution and subsequently affects the recombination losses are still unknown. Recently, Scardera *et al.* extended the specific surface area (SSA) concept, typically used for nanoparticles, to surface textures with nanofeatures. SSA was defined as the ratio of the surface area to the volume of the nanofeature. It was found that the measured sheet resistance (R_{sheet}) of the b-Si emitter was independent of both the surface area and the surface morphology, but exhibited a strong correlation with SSA [26]. However, current one-dimensional (1-D) and 2-D R_{sheet} theories based on the dopant concentration cannot fully explain such an outcome [26] and, thus, it is doubtful whether the R_{sheet} measured by the four-point-probe method is a reliable indicator for comparing b-Si doping levels.

Manuscript received November 9, 2021; revised January 20, 2022; accepted January 28, 2022. This work was supported by Australian Renewable Energy Agency under Grant 2017/RND007 and Grant 2017/RND009. *(Corresponding authors: Malcolm Abbott; Bram Hoex.)*

Shaozhou Wang, Giuseppe Scardera, Fa-Jun Ma, Yu Zhang, Malcolm Abbott, and Bram Hoex are with the University of New South Wales, Sydney, NSW 2050, Australia (e-mail: shaozhou.wang@unsw.edu.au; gscardera@gmail.com; f.ma@unsw.edu.au; yu.zhang@unsw.edu.au; m.abbott@unsw.edu.au; b.hoex@unsw.edu.au).

David Payne is with the Macquarie University, Sydney, NSW 2109, Australia (e-mail: david.payne@mq.edu.au).

This article has supplementary material provided by the authors and color versions of one or more figures available at https://doi.org/10.1109/JPHOTOV.2022.3148713.

Digital Object Identifier 10.1109/JPHOTOV.2022.3148713

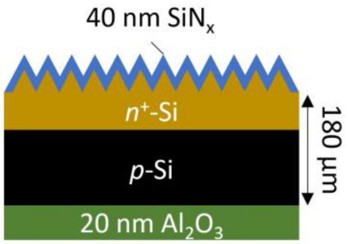

Fig. 1. Schematic of the simulated structure with the front-side texture, the front-side n^+ diffused region, the front-side SiN$_x$ passivation layer and the rear-side Al$_2$O$_3$ passivation layer.

A comprehensive investigation into the effect of nanoscale surface morphologies on b-Si electrical properties will be shown in this article. We will investigate the POCl$_3$-diffused front-junction device structure which, for example, is used in the industry-dominant passivated emitter and rear cell (PERC). We will present a systematic 3-D nanoscale simulation approach, corroborated using experimental results, to investigate the POCl$_3$ diffusion and the corresponding electrical performance. We will show how the b-Si nanofeature size influences the doping profile. We will investigate the characteristics of lateral conductance in the b-Si emitter and the correlation between the measured b-Si R$_{\text{sheet}}$ and the doping level. We will subsequently examine the emerging role of SSA optimization in suppressing emitter Auger recombination, Shockley–Read–Hall (SRH) recombination, and the doping-related surface recombination by investigating the emitter saturation current density (J$_{0\text{e}}$). Finally, the simulation results will be compared with empirical results, and the effects of nanofeature size on the optical performance will be discussed as well.

II. Methodology and Modeling

A. Simulation Overview and Experiment Information

In this article, the 3-D numerical simulations were performed using the process simulation module[27] and the device simulation module [28] in Synopsys Sentaurus TCAD, which solves the fully coupled set of differential equations based on the transport models (the charged-pair dopant transport model for diffusion simulations and the drift-diffusion carrier transport model for device simulations). The front-side POCl$_3$ diffusion simulations were simplified as the nonmoving-boundary processes using the two-phase segregation model, i.e., the phosphorus atoms diffused from the 40 nm phosphosilicate glass (PSG) layer into the 180 μm p-type Si substrate directly without the *in-situ* Si etching. Hence, the surface morphology will not be modified after the diffusion. The PSG layers were then removed and the emitter surfaces were covered with uniform 40 nm SiN$_x$ passivation layers. Also, the rear undiffused planar surfaces were covered with uniform 20 nm Al$_2$O$_3$ passivation layers for the subsequent device simulations, as shown in Fig. 1. The simulations of the electrical performance were based on the drift-diffusion carrier transport model with the 3-D Poisson's equation, Fermi–Dirac statistics, Schenk's band gap narrowing model [29] and Philips unified mobility model [30]. For the R$_{\text{sheet}}$ simulations, the current injection had a 0.01 V contact potential difference. For the J$_{0\text{e}}$ simulations, the optical injection was under quasi-steady-state conditions with a uniform generation. The simulated unit sample had a full-size thickness (180 μm) while the length and width were modelled in the nanoscale, i.e., the unit sample was a long bar extending along with the entire wafer thickness. The full-size sample simulation was achieved by setting periodical boundaries for the unit sample side-walls. More simulation details are listed in the Supplementary Material, and the models used in this article will be discussed in the following sections.

The experiment results used in this article were reproduced from our previous work [26]. The b-Si samples were fabricated by 2-min and 16-min reactive-ion etching (RIE-2min and RIE-16min) using an SPTS Pegasus System. The nanofeatures were assumed to be conical. The modeling dimensions were based on the measured surface areas and nanofeature height distributions using a Bruker ICON Atomic Force Microscope. The diffusion recipes used in the simulations were identical to the ones used in the experiments, i.e., an 865 °C nonoxidation recipe [26]. The doping profiles of planar samples were measured by Time-of-Flight Secondary Ion Mass Spectrometry (ToF-SIMS) using an IonTOF TOF.SIMS 5 and also measured by electrochemical capacitance voltage (ECV) profiling using a WEP CPV21 ECV-Profiling. Field-emission scanning electron microscope (SEM) measurements also confirmed the surface morphology and the 2-D doping distributions were monitored with SEM dopant contrast imaging (SEMDCI) using an FEI Nova NanoSEM 450 system. The R$_{\text{sheet}}$ samples were measured by the four-point-probe method using a Sunlab Sherrescan. The surface reflectance was measured by the spectrophotometer using a PerkinElmer 1050. More experiment details can be found in [26].

B. Diffusion Modeling

In the POCl$_3$ diffusion simulations, the charged-pair diffusion model, which is one of the widely used models [31], solved the continuity equations for the charged dopant-defect pairs, i.e., phosphorus-vacancy (PV) and phosphorus-interstitial (PI) pairs with various charge states [27]. It can be generally expressed as

$$\frac{\partial C_P^{\text{total}}}{\partial t} = \nabla \cdot \sum_{c,\,X} D_{PX^c}\left(\frac{n}{n_i}\right)^{-c-1} \nabla\left(C_P^{\text{active}} k_X \frac{n}{n_i}\right) \tag{1}$$

where C_P^{total} is the total P concentration, D_{PX^c} is the effective diffusivity of PV or PI pairs (defect X is V or I) at defect charge state c, n is the electron density, n_i is the intrinsic carrier density, and k_X is the coefficient determined by the defect concentration. The electrically active P concentration C_P^{active} was determined by the solid dopant activation models [27]

$$C_P^{\text{active}} = \frac{f C_P^{\text{SS0}} C_P^{\text{total}}}{f C_P^{\text{SS0}} + C_P^{\text{total}}} \tag{2}$$

$$C_P^{\text{SS0}} = 1.85 \times 10^{22} \times e^{\frac{-0.27}{k_B T}} \tag{3}$$

where C_P^{SS0} is the solid solubility of P in an Arrhenius equation, k_B is the Boltzmann constant, T is the temperature ($k_B T$ in eV), and the multiplication factor $f = 2.5$ is a fitting parameter. It

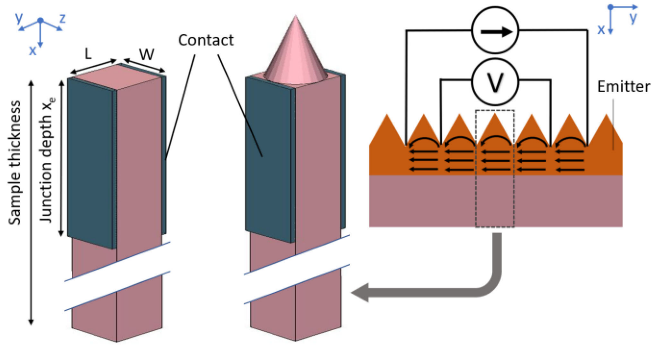

Fig. 2. Schematics of planar and nanofeature unit wafers illustrating the parallel-contact method used for sheet resistance simulations. The parallel-contact method mimics the current injection for a unit wafer in the four-point-probe measurement.

should be noted that the solubility limit used in this article could be relatively high due to the lack of measured surface dopant concentration. The C_P^{active} in the heavily doped surface was assumed according to the doping profile fitting. It was assumed that the inactive P was the interstitial P atom as a single type of defect and its concentration can be calculated by

$$C_P^{\text{inactive}} = C_P^{\text{total}} - C_P^{\text{active}}. \tag{4}$$

C. Sheet Resistance Modeling

The sheet resistance R_{sheet} implies the characteristic lateral conductance for the emitter. The first principle definition of R_{sheet} for planar semiconductors is

$$R_{\text{sheet}} = \frac{1}{\int_0^{x_e} q\left(\mu_n n + \mu_p p\right)\, dx} \tag{5}$$

where n and p are the electron and hole densities, μ_n and μ_p are the carrier mobilities, and x_e is the depth from the surface ($x = 0$) to the metallurgical junction. However, (5) can only determine the local R_{sheet} in 1-D. Therefore, it should be extended to a 3-D equation to calculate the average R_{sheet} for a b-Si emitter

$$\bar{R}_{\text{sheet}} = \frac{\iint R_{\text{sheet}}\left(y, z\right)\, dy\, dz}{A_{proj}} \tag{6}$$

where A_{proj} is the projected area of the b-Si surface. $\bar{R}_{\text{sheet}}$ can be regarded as an average value of calculated R_{sheet} based on the dopant distribution. Moreover, we propose a novel parallel-contact simulation method to determine the effective R_{sheet}, which mimics the one-direction lateral current injection in the four-point-probe measurement. As shown in Fig. 2, this method was based on the fundamental lateral resistance equation for a cuboid emitter

$$R = \bar{\rho}\ \frac{L}{x_e W} = R_{\text{sheet}}\ \frac{L}{W} \tag{7}$$

where $\bar{\rho}$ is the average resistivity, L is the length, and W is the width. The depth of the side-wall contact was identical to the depth of the metallurgical junction x_e. According to (5), it can be derived that $R_{\text{sheet}} = \bar{\rho}\ /x_e$, thus, the lateral resistance R will be equal to R_{sheet} when $L = W$. In this way, the one-direction lateral current could be injected into the unit wafer and the measured lateral resistance was independent of the size of the unit wafer. This method can be extended to a b-Si unit wafer. However, the injected current will be multidirectional within the nanofeature. Virtual contacts, in which the contact resistance is zero and contact recombination velocities equal to the carrier thermal velocities, were used in the parallel-contact simulations.

D. Emitter Saturation Current Density Modeling

The emitter saturation current density J_{0e} was used to evaluate the recombination losses. In this article, J_{0e} was determined by the lifetime conversion method (known as Kane and Swanson's method) under the conductive boundary assumption, i.e., the carrier generation in the emitter region was negligible, and the emitter and surface regions were lumped as a conductive boundary [32]. The standard equation is

$$\frac{1}{\tau_{eff}} - \frac{1}{\tau_{\text{base}}} - \frac{1}{\tau_{\text{SRV},r}} = \frac{1}{\tau_e} = J_{0e}\ \frac{\left(N_{dop} + \Delta n\right)}{qWn_{i,eff}^2} \tag{8}$$

where τ_{eff} is the effective lifetime, τ_{base} is the base lifetime, which is determined by the base SRH, Auger, and radiative recombination losses $\tau_{\text{SRV},r}$ is the rear surface lifetime, which is determined by the rear surface recombination velocity (SRV) and carrier densities, τ_e is the lumped front boundary lifetime determined by the recombination losses in the emitter and the corresponding surface, N_{dop} is the base doping, Δn is the excess carrier concentration in the flat-band region, $n_{i,eff}$ is the effective intrinsic carrier density, and W is the wafer thickness. Since the total J_{0e} is a combination of the effective recombination mechanisms in the boundary

$$J_{0e} = J_{0e,\text{Auger}} + J_{0e,\text{SRH}} + J_{0e,\text{SRV},f} \tag{9}$$

these recombination components $J_{0e,x}$ can be individually calculated by the corresponding average recombination rates $\bar{U}_{e,x}$ in the emitter region, based on (8) and given that $\tau_{e,x} = \Delta n/\bar{U}_{e,x}$

$$J_{0e,x} = \frac{\bar{U}_{e,x} qWn_{i,eff}^2}{\Delta n\left(N_{dop} + \Delta n\right)}. \tag{10}$$

For the Auger component $J_{0e,\text{Auger}}$, the recombination rate $U_{e,\text{Auger}}$ was determined from Richter's model [33]. For the SRH component $J_{0e,\text{SRH}}$, it was assumed that the emitter SRH recombination was only caused by the inactive P as a single type of defect. The recombination rate $U_{e,\text{SRH}}$ was determined by

$$U_{e,\text{SRH}} = \frac{C_P^{\text{inactive}} v_{the} v_{thh} \sigma_n \sigma_p \left(np - n_{i,eff}^2\right)}{v_{the}\sigma_n\left(n + n_1\right) + v_{thh}\sigma_p\left(p + p_1\right)} \tag{11}$$

where v_{the} and v_{thh} are the carrier thermal velocities, σ_n and σ_p are the carrier capture cross sections, and n_1 and p_1 are the thermal emission of carriers from the defect energy. Given that $n + n_1 \gg p + p_1$ for an *n*-type emitter and $n \gg n_1$ due to the negligible thermal emission, (11) can be simplified as

$$U_{e,\text{SRH}} \approx \frac{C_P^{\text{inactive}} v_{thh} \sigma_p \left(np - n_{i,eff}^2\right)}{n}. \tag{12}$$

It was assumed that the σ_p for the inactive P was 7.5×10^{-18} cm^2[34]. For the surface component $J_{0e,\mathrm{SRV},f}$ with the heavily doped n-type surface as well as the high-fixed-charge accumulation condition, the surface recombination rate $U_{e,\mathrm{SRV},f}$ was mainly determined by the intrinsic surface recombination velocity of the minority carrier (S_{p0}) and the surface minority carrier density (p_s) based on the SRH model for a single defect energy [35]

$$U_{e,SRV,f} = \frac{p_s n_s - n_{i,eff}^2}{\frac{p_s+p_1}{S_{n0}} + \frac{n_s+n_1}{S_{p0}}} \approx S_{p0} p_s \qquad (13)$$

where the S_{p0} depended on the surface active P concentration $C_{P\ surf}^{\mathrm{active}}$ and it was parameterized by Altermatt's model [36].

III. RESULTS AND DISCUSSION

A. Enhanced Area Factor and Specific Surface Area for Black Silicon

The ratio of the surface area (the lateral surface area of a cone) to the projected area (the base circle area of a cone), or enhanced area factor (EAF), is the most widely used morphology parameter in qualifying the b-Si electrical performance. The total number of surface defects and the diffused silicon area will scale with EAF, thus enhancing defect recombination at the enlarged surface as well as Auger recombination in the emitter. However, in our previous work, we showed that nanofeatures of different sizes could have an identical EAF but exhibit significantly different postdiffusion $\mathrm{R_{sheet}}$ values, and that in some cases, such values were independent of EAF [26]. Therefore, employing a better metric to evaluate nanofeature sizes is essential for b-Si studies.

In this article, we used SSA to quantify the nanofeature size. It is defined as the ratio of the nanofeature surface area to the nanofeature volume [26], where a larger nanofeature will have a smaller SSA for a given EAF condition, as shown in Fig. 3(a). Fig. 3(b) shows the effects of conical nanofeature base radii and heights on the SSA values. As SSA is a relative size metric associated with the surface area, it would be more meaningful to investigate the nanofeatures with different SSA values but similar EAF values when studying the effects of sizes. Typically, the b-Si surfaces applied in solar cells will have an EAF ranging from 2 to 10 [1], [19], [37]. We assumed that RIE textures were composed of conical nanofeatures, and as a result, the SSA was in a range from around 10 μm^{-1} to 430 μm^{-1}, as shown in Fig. 3(b). In this article, we referred to shallow RIE b-Si textures as those having small nanofeatures with a height of $<$ 100 nm and an SSA of $>$ 100 μm^{-1}, referred to moderate RIE b-Si textures as those having moderate nanofeatures with a height of 100 nm–300 nm and an SSA of 20 μm^{-1}–100 μm^{-1}, and referred to deep RIE b-Si textures as those having large nanofeatures with a height of $>$ 300 nm and an SSA of $<$ 20 μm^{-1}.

B. Effects of Nanofeature Size on Doping Profile

This section will discuss how the nanofeature sizes influence doping by investigating the doping profiles of planar reference, RIE-2min and RIE-16min samples. In our previous work, we find that the b-Si $\mathrm{R_{sheet}}$ measured by the four-point-probe method increases with an increasing nanofeature size. Diffusion simulations also indicate that a larger conical nanofeature has a higher concentration of active P dopant C_P^{active} at the tip and lower doping at the base of the nanofeature. We propose that there will be limited current flowing in the heavily doped tip of the nanofeature. Thus, the doping level in the underlying substrate plays an essential role in the lateral emitter conductance [26]. The detailed simulation results and analysis for this finding will be shown in Section III-C. This section will revisit the diffusion simulations of the conical nanofeatures and provide a more detailed analysis of both the active and inactive P atom distributions. This analysis will then be extended to investigate the lateral conductance (see Section III-C) and recombination behaviors (see Section III-D) of conical nanofeatures. The nanofeature dimensions, EAF and SSA of the investigated b-Si samples are shown in Fig. 3(b). The nanofeature dimensions used for these simulations were based on the height and slant angle distributions determined from atomic force microscope (AFM) [26].

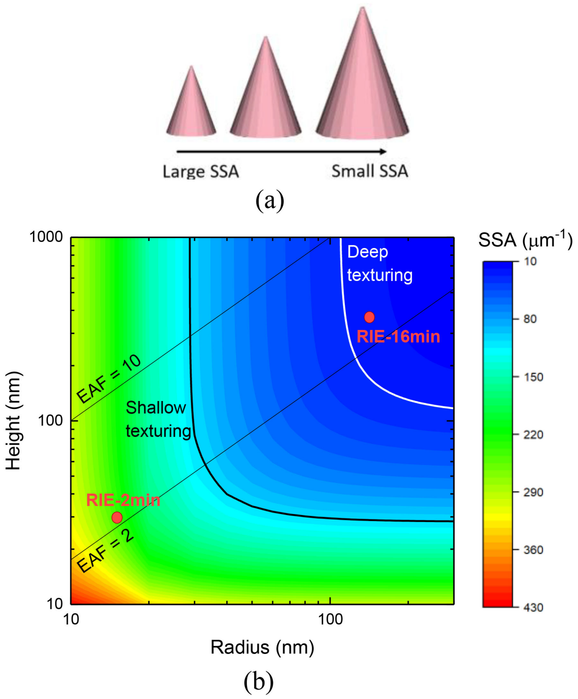

Fig. 3. (a) Schematics of nanofeatures with the same EAF but different SSA, i.e., the nanofeatures have the same aspect ratio but an increasing height, which results in a decreasing SSA. (b) SSA values for conical nanofeatures with varying base radii and heights. The regions defined as shallow texturing and deep texturing are indicated. The locations of the simulated RIE-2min and RIE-16min conditions are also indicated.

Fig. 4(a)–(c) shows the cross-sectional SEMDCI results along with the corresponding simulated C_P^{active} distributions for the planar, RIE-2min and RIE-16min conditions, respectively. The RIE conditions both exhibit heavily doped near-surface regions as well as deeper metallurgical junction depths compared to the planar sample. Furthermore, the shallow texture (RIE-2min) has a higher doping level in the underlying substrate and a deeper junction depth compared to the deep texture (RIE-16min).

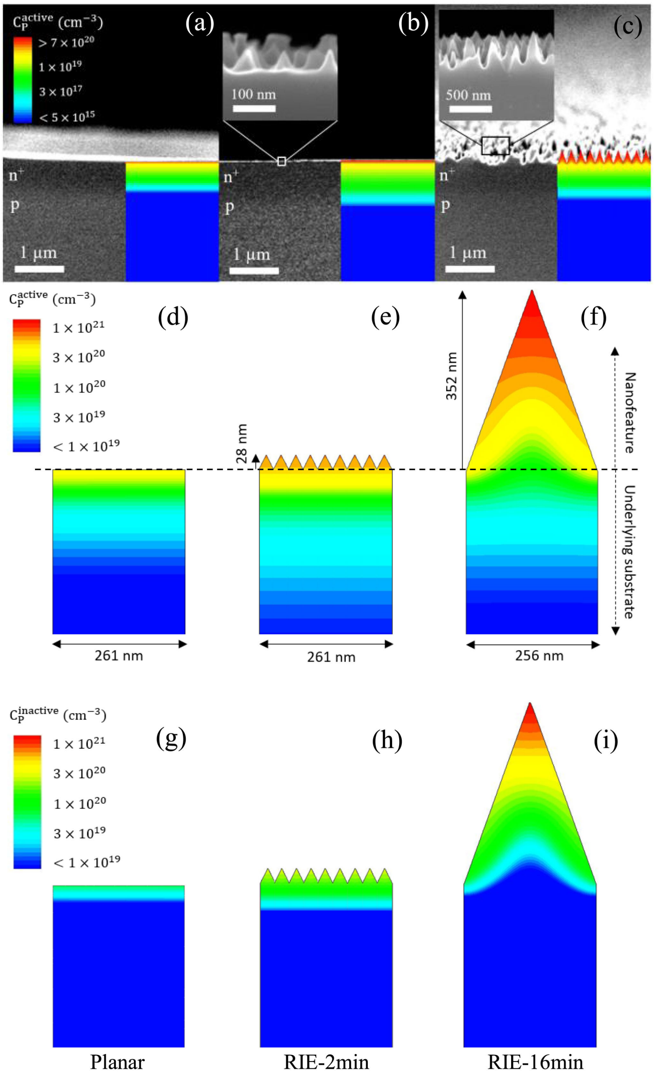

Fig. 4. Cross-sectional SEMDCI for (a) planar reference, (b) RIE-2min, and (c) RIE-16min samples, which illustrate the junction depth. The inset SEM images show the as-textured surface morphologies of b-Si samples. The cross-sectional results from simulations are also shown on the same scale for comparisons. Zoom-in of the simulated active and inactive P concentration (C_P^{active} and C_P^{inactive}) cross-sectional profiles for planar reference [(d) and (g)], RIE-2min [(e) and (h)], RIE-16min [(f) and (i)] samples in the heavily doped near-surface regions.

Fig. 4(d)–(f) shows the simulated C_P^{active} distributions in the heavily doped near-surface regions. The simulation results indicate that the nanofeature size has a significant effect on the dopant distribution. The heavily doped nanofeature has relatively uniform doping for the shallow b-Si texture (RIE-2min). On the other hand, for the deep b-Si texture (RIE-16min), the doping level increases significantly from the bottom to the peak of the nanofeature, resulting in an extremely high dopant concentration at the tip region. This can be attributed to the diffusion length of the P atoms not being sufficient to reach the bottom of the nanofeature. In addition, the dopants diffused from the side-wall will perturb the diffusion process. The diffusion of P atoms in the heavily doped region relies on charged vacancies. Since the P concentration at the tip will be much larger than the concentration of charged vacancies in the nanofeature (the P atoms from the side-wall will also diffuse to the tip), the P atoms at the tip will not efficiently diffuse. Consequently, there will be a dopant accumulation in the tip region. This leads to the number of dopants diffused into the underlying substrate being lower. Therefore, the metallurgical junction depth with reference to the bottom of the deep texture (RIE-16min) is more shallow than that of the shallow texture (RIE-2min), even though the RIE-16min sample has a larger EAF.

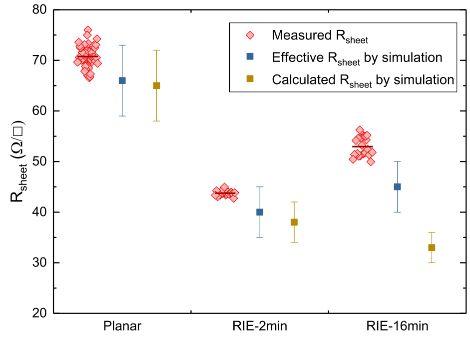

Fig. 5. Simulated and measured sheet resistance R_{sheet}. The experiment results were reproduced from [26] and the average values for each set of data are indicated. The effective R_{sheet} was determined by the parallel-contact simulation. The calculated R_{sheet} by the first principle is the average of local R_{sheet} values of each b-Si sample determined by (6). Since the ECV measurement had a maximum ±4.3% error and the result of diffusion simulation had a ±6.2% uncertainty due to the profile fitting error and the uncertainty of the surface dopant concentration, it is assumed that the simulated sheet resistance result will have a ±10.5% uncertainty, as shown by error bars.

Fig. 4(g)–(i) shows the corresponding distributions of inactive P atoms. The b-Si samples have a wider distribution of inactive P atoms and also higher inactive P concentrations C_P^{inactive} in the emitters than the planar reference sample. In addition, compared to the shallow texture (RIE-2min), the C_P^{inactive} of the deep texture (RIE-16min) is generally larger and the C_P^{inactive} in its tip region is an order of magnitude higher at around 1×10^{21} cm^{-3}. This can be attributed to the P atom accumulation in the tip region and the P solubility limit. A region with a high concentration of inactive P atoms is known as a "dead layer", where the high concentration of inactive P is in the form of interstitial P atoms, inactive P clusters and SiP precipitates. As we do not know the fractions of such components in the "dead layer", it is assumed that the inactive P atoms are a single type of effective defect with a hole capture cross-section $\sigma_p = 7.5\times10^{-18}$ cm^2 [34]. This assumption will be employed later in Section III-D when investigating SRH recombination loss due to such defects.

C. *Effects of Nanofeature Size on Sheet Resistance*

In this section, we will investigate the effects of nanofeature sizes on the sheet resistance R_{sheet}. Fig. 5 shows the measured R_{sheet} from four-point-probe measurements, the corresponding simulation results of the effective R_{sheet} determined using the parallel-contact method, and the calculated R_{sheet} values based on the simulated dopant distributions using (6). It can be seen that the b-Si samples had a lower measured R_{sheet} than the planar reference sample and that the shallow texture (RIE-2min)

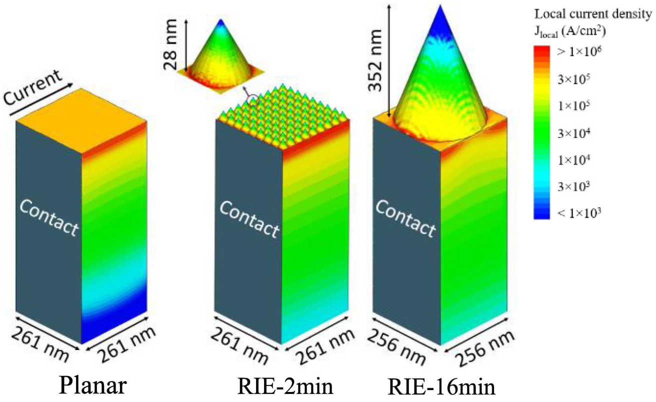

Fig. 6. Simulated local current density J_{local} of planar, RIE-2min and RIE-16min samples by the parallel-contact method.

has the lowest measured R_{sheet}. The simulation results by the parallel-contact-method show a relatively good agreement with the experiment results. However, the R_{sheet} of the deep texture (RIE-16min) calculated using (6) has a significant discrepancy with the corresponding experiment result and it incorrectly predicts that the R_{sheet} of the RIE-16min sample would be lower than the RIE-2min sample. This can be attributed to the dopant distribution, as discussed in Section III-B, i.e., the planar sample has the lowest dopant concentration while the RIE-16min sample has the highest doped nanofeatures with a large volume. However, the shallow texture (RIE-2min), in fact, had the lowest measured R_{sheet}. This implies that the dopant concentration can not simply explain the measured R_{sheet} results.

Fig. 6 shows the simulated local current density J_{local} of the planar and b-Si samples during current injection in the parallel-contact method with 0.01 V contact potential difference. For all cases, it can be seen that most of the current flow through the top portion of the underlying substrate and the J_{local} decreases with increasing depth into the substrate. This is caused by the reduction of dopant concentration, as shown in Fig. 4, and consequently, the corresponding conductivity decreases. Contrarily, although the dopant concentration is relatively high in the nanofeatures, the J_{local} decreases as the height increases and reaches the lowest value at the tip of the nanofeature. Fig. 7 shows the line scans inside the nanofeatures from the tips to the underlying substrate. These results confirm the strong correlation between the J_{local} and the dopant concentration in the underlying substrate for all samples. However, the J_{local} has a dramatic decrease in the nanofeature even though the dopant concentration keeps increasing from the bottom to the tip of the cone. The extremely low J_{local} in the tip regions can be explained by the current path length in the 3-D structure, i.e., the current will not always take the path with the highest dopant concentration (where the conductivity is the highest) since the total conductance is a function of the conductivity and the path length. It can be concluded that the doping level in the underlying substrate predominantly determines the effective lateral conductance and the effective R_{sheet} of a b-Si emitter, regardless of the doping level in the nanofeature. This can explain the significant difference between the calculated and effective R_{sheet} for the large nanofeature (RIE-16min) in Fig. 5. This also explains why the difference of the calculated and effective R_{sheet} is, to the contrary, insignificant for the RIE-2min sample where the volume of the heavily doped nanofeature is much smaller than that of the underlying emitter. Moreover, the simulation results reveal that the effective R_{sheet} acquired from the four-point-probe method is predominantly an indicator of the doping level in the underlying substrate below the nanofeature.

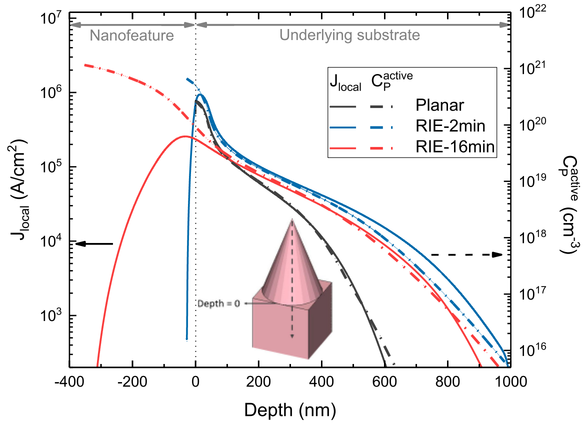

Fig. 7. Line scans for local current density J_{local} and dopant (active phosphorus) concentration starting from the surface of the planar sample and the tips of nanofeatures to the metallurgical junction depths, which show the correlation between the J_{local} and the dopant concentration. A depth = 0 corresponds to the interface between the base of a nanofeature and the underlying substrate.

D. Effects of Nanofeature Size on Emitter Saturation Current Density

In this section, we will study the effects of nanofeature size on each recombination mechanism by investigating the J_{0e} of simulated samples with a lifetime structure, as shown in Fig. 1. We will investigate a wide range of cone sizes from the nanoscale to the microscale. To eliminate the effects of surface area, all cones had a fixed EAF = 2.2. Fig. 8 shows the simulated J_{0e} results, including the fractions of different recombination mechanisms. The smallest nanofeature sample (SSA = 232 μm^{-1}) and the planar reference sample show a very similar J_{0e} result. The largest microfeature condition (SSA = 3 μm^{-1}) has a 2 μm height, which is close to the surface morphologies fabricated with conventional texturing methods. Fig. 8 indicates that as the nanofeature size increases, the total recombination loss rises. When the cone size is increased to the microscale, the highest J_{0e} = 178 fA/cm^2 was obtained, which is smaller than the theoretical highest J_{0e} = 206 fA/cm^2 calculated from the product of the planar reference J_{0e} and the EAF value. Such a lower result is also observed in micropyramidal samples. McIntosh and Johnson reviewed the reported J_{0e} values for micropyramidal samples and found that the J_{0e} increased with a factor < 1.73 (the EAF for pyramidal textures) for heavily diffused samples (planar reference $R_{sheet} < 100$ Ω/□). This was attributed to a nonconformal emitter region [38], which is consistent with the simulation results presented in this section. It should be noted that since we only focus on the dopant-associated recombination caused by the morphology variation, the effects of the crystal

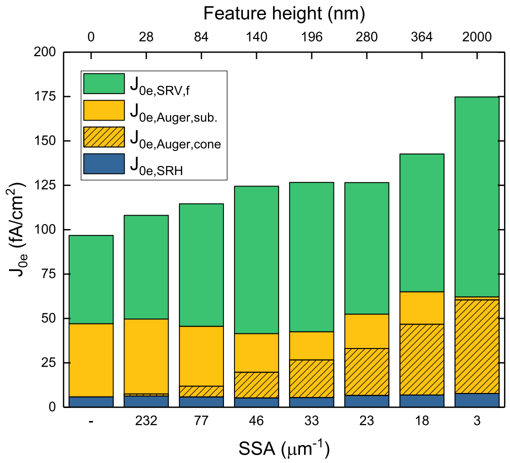

Fig. 8. J_{0e} components for varying cone sizes. The EAF value was fixed at 2.2 for all cones on the textured surfaces. It was assumed that the local S_{p0} at the Si-SiN$_x$ interface depends on the surface dopant concentration $C^{active}_{P\ surf}$. The Auger components in the cone and underlying substrate are also individually shown.

orientations and the surface stress on the recombination losses were not considered in this article. Fig. 9(a) shows the average P concentration in the nanofeatures and the underlying substrate, which relates to the SRH and Auger recombination losses. As the nanofeature size increases, the total P concentration decreases for the nanocone region and the underlying substrate region. Fig. 9(b) shows the corresponding number of P atoms of Fig. 9(a) calculated for the same unit sample dimensions with an identical projected area (380 nm × 380 nm), which reveals the effects of the nanofeature volume on the P distribution. It is indicated that as the nanofeature size increases, the total number of P atoms decreases in the underlying substrate region while the number in the nanocone increases.

Fig. 8 indicates that the SRH recombination loss due to the inactive P atoms is insignificant even though the inactive P concentration is high in the nanofeature, as shown in Fig. 4. This results from the strong charge carrier population control in the heavily doped nanofeature, i.e., the minority carrier density available for SRH recombination is very low due to the high doping level and the carrier consumption by Auger recombination and surface recombination.

Moreover, Fig. 8 also reveals the influence of nanofeature size on the Auger recombination. When the surface texture is relatively shallow (SSA $> 77\ \mu$m^{-1} and height < 84 nm), the predominant Auger recombination occurs in the underlying substrate with a relatively high dopant concentration. When the nanofeature size increases, the Auger recombination loss in the nanocone $J_{0e,Auger,cone}$ rises with an increasing proportion of the nanofeature J_{0e}. This can also be attributed to the effects of the nanofeature volume, i.e., the increasing nanofeature volume leads to the increasing total number of dopants in this region, as shown in Fig. 9(b). Therefore, there is more Auger recombination occurring in the nanofeature. However, to achieve the lowest total Auger recombination loss, the nanofeature size should be moderate to balance the Auger recombination losses in the nanofeature and the underlying substrate. The optimal nanofeature size with the lowest Auger recombination loss in this article with an EAF of 2.2 had a SSA $= 46\ \mu$m^{-1} and height $= 140$ nm.

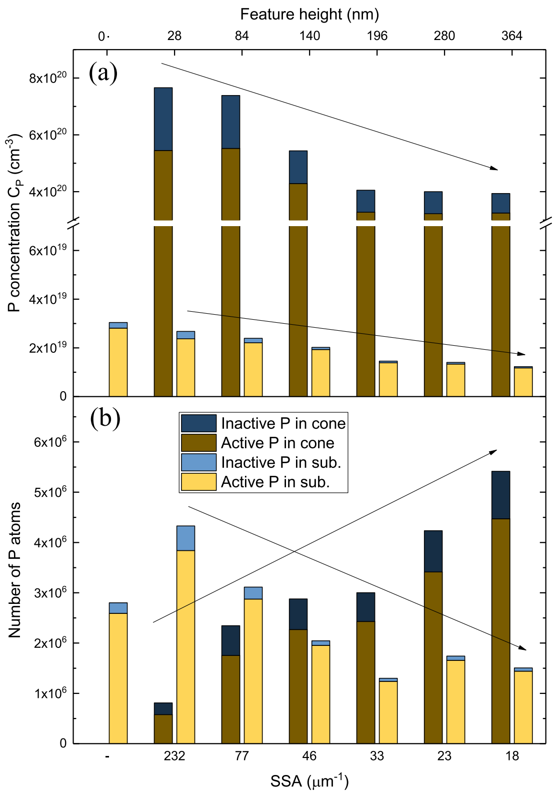

Fig. 9. (a) P concentrations in the nanofeatures (nanocones) and underlying substrates of the simulated samples shown in Fig. 8 and (b), the corresponding number of P atoms for a fixed projected area of 380 nm × 380 nm. The extracted values of underlying substrates were in the region from the top of the substrate to the depth of the metallurgical junction. The EAF values were fixed at 2.2 for all textured samples. The arrows indicate the trends as the nanofeature size increases (SSA decreases).

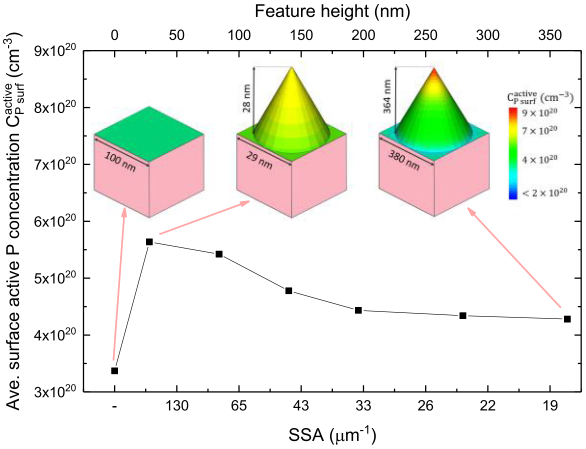

Fig. 10. Effect of nanofeature size on average surface dopant concentrations. The inset graphs show the concentrations of the local dopant on the surfaces of planar, small nanofeature (SSA $= 232\ \mu$m^{-1}) and large nanofeature (SSA $= 18\ \mu$m^{-1}). The EAF value was fixed at 2.2 for all textured samples.

Fig. 10 shows the effects of nanofeature size on the surface active P concentrations $C^{active}_{P\ surf}$, which relate to the

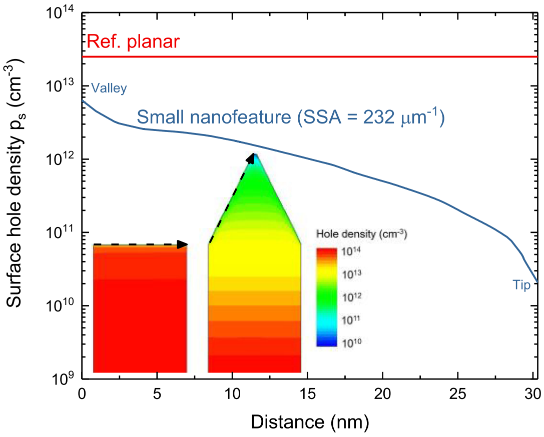

Fig. 11. Simulated surface hole density p_s of planar reference and b-Si samples with small nanofeatures at 5×10^{16} cm^{-3} injection condition. The *x*-axis is the distance from the valley to the tip of nanofeature. The cross-sectional hole distributions are also shown.

surface recombination loss. The average $C_{P\ surf}^{\text{active}}$ decreases as the nanofeature size increases, which means there will be an effective surface dopant enhancement only when the nanofeature size is sufficiently small, even though the $C_{P\ surf}^{\text{active}}$ was extremely high at the tip region for the large nanofeature. Fig. 11 shows the corresponding surface minority carrier density p_s of Fig. 10 for the planar reference and a small nanofeature case (SSA = 232 μm^{-1}). It indicates that the p_s at the nanofeature surface is much lower than the planar reference and a lot lower than the expectation according to the increase in surface doping shown in Fig. 10. In particular, p_s is reduced by over three orders of magnitude in the tip of the nanofeature. This can be attributed to the fact that the doping profile is significantly deeper from the nanofeature surface than from the planar surface, resulting in a more effective carrier population control [39]. This is similar to the enhanced charge-assisted carrier control by the effective space charge region compression for the lightly doped b-Si samples [17]. The decrease in p_s at the nanofeature surface more than compensates for the increase in S_{p0} at the highly doped surface and, subsequently, the surface recombination loss determined by the product of p_s and S_{p0} (13) increases with a factor less than the EAF. This explains why the $J_{0e,SRV,f}$ of the small nanofeature is comparable to that of the planar reference sample in Fig. 8. As the nanofeature size increases, this effect will become less pronounced, and $J_{0e,SRV,f}$ will start to scale with EAF.

It can be concluded that the surface morphology optimization strategy will depend on the diffusion level and surface passivation performance. For the heavily-doped b-Si emitters with predominant Auger recombination loss, a moderate nanofeature (SSA = 46 μm^{-1} and height = 140 nm) size is beneficial as such a size will contribute to the reduction of the total Auger recombination loss from 41 fA/cm^2 for the planar reference to 36 fA/cm^2 for the b-Si sample. For the b-Si emitters with comparable Auger recombination and surface recombination losses, such as the example shown in Fig. 8, the simulation results indicate that a low total recombination loss will be achievable when the nanofeature is small, i.e., 108 fA/cm^2 for the b-Si sample with EAF = 2.2 compared to 97 fA/cm^2 for the planar reference.

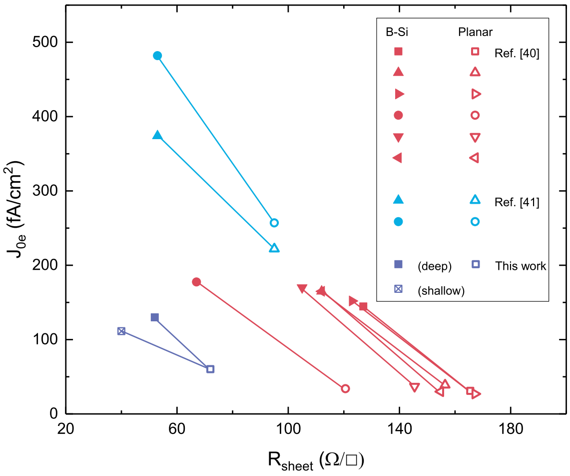

Fig. 12. Electrical performance comparison of b-Si emitters and planar reference emitters. The b-Si samples of reported results are $POCl_3$-diffused deep RIE texture (SSA < 20 μm^{-1}) with large surface areas (EAF > 4) passivated by corona-charge-enhanced ALD-Al_2O_3 or ALD-SiO_2/Al_2O_3 stacks [40], [41]. The simulated b-Si samples have a low EAF = 2.2 and different SSA (SSA = 232 μm^{-1} for the shallow nanocone and SSA = 18 μm^{-1} for the deep nanocone) and are passivated by SiN_x with $Q_f = 5\times10^{12}$ cm^{-2}.

E. Optimization of B-Si Emitters

In this section, we will compare the electrical performance and optical performance of reference and the RIE b-Si samples. We will also discuss the potential influences of b-Si nanofeature size on the performance of solar cells.

The effects of surface nanotexture on the dopant-related electrical properties (R_{sheet} and J_{0e}) for various diffusion recipes are shown in Fig. 12. These empirical b-Si results were for a deep RIE nanotexture with large surface nanofeatures (SSA < 20 μm^{-1}). It should be noted that the field-effect passivation in these b-Si and planar reference samples was enhanced by corona charge deposition. Therefore, the surface recombination losses were relatively low and the predominant J_{0e} component was due to Auger recombination. Fig. 12 shows that when an identical diffusion recipe is employed for b-Si and planar reference samples, the nanotextured sample will have a higher J_{0e} but a lower R_{sheet}, which results from the doping enhancement in the b-Si emitter as discussed in Sections III-B–III-D. According to the comparison of the J_{0e}-R_{sheet} slopes, it can be found that the effects of diffusion recipes on the electrical properties for the large-nanofeature b-Si are very similar when R_{sheet} of the planar reference samples are < 180 Ω/□, i.e., the ratios of the R_{sheet} reduction and the corresponding J_{0e} increase are similar for all cases. It should be noted that although the diffusion recipe used in the simulations causes heavier doping and thus the simulated R_{sheet} is lower than those from the literature, the simulated J_{0e} is lower than the empirical J_{0e} as the simulated cones have a lower EAF and consequently lower surface recombination loss. Moreover, the simulation results reveal that the R_{sheet} can be further reduced with an even lower degree of J_{0e} increase by using a shallow b-Si texture. As discussed in Sections III-C and III-D, this is plausible given that a relatively small nanofeature ($\text{SSA} > 20\ \mu\text{m}^{-1}$) can enhance the doping in the underlying substrate region, which relates to the lateral conductance improvement directly. Although this will also increase the Auger recombination compared to the planar reference emitter to some extent, it will be still lower than that for a heavily doped large nanofeature.

It should also be noted that the optical performance of shallow nanofeatures would need to be verified before incorporating them into a solar cell. Ideally optical simulations of our simulated nanocone features would be performed, but such investigations are beyond the scope of this article. However, we have previously shown that while deep RIE textures do exhibit very low weighted average reflectance (WAR), RIE texture with an EAF of 2.3, which is close to the EAF of our simulated shallow nanotexture, exhibited a significantly lower WAR than random pyramids (RPD) [26]. Although a deep RIE nanotexture with large EAF can have a near-zero reflectance without antireflection coating, the collection efficiency could be problematic [40], which outweighs the optical gains and leads to a low external quantum efficiency [42]. On the other hand, a shallow nanotextured can be combined with a microtexture to form a hierarchical structure which has a better optical performance and also a high collection efficiency [43]–[45]. As such, any final optimization strategy should consider all aspects for the development of high-efficiency front-junction b-Si solar cells.

IV. CONCLUSION

The effects of nanofeature sizes on the electrical performance of b-Si emitters were investigated by numerical simulations using Synopsys Sentaurus TCAD. It was revealed that the surface nanotexture would lead to a doping enhancement in the underlying substrate region for small nanofeatures. However, such enhancement will be suppressed for large nanofeatures, while there will be an extremely high dopant concentration within such nanofeatures, especially at the tip region. It was subsequently found that this heavily doped nanofeature will barely affect the lateral conductance during a R_{sheet} measurement by the four-point-probe method. The lateral conductance is mainly determined by the doping level in the underlying substrate region. Hence, this can explain why Scardera *et al.* [26] observed that the measured R_{sheet} will be smaller as the nanofeature size decreases. This also indicates that the measured R_{sheet} by the four-point-probe method can be regarded as mainly an indicator of underlying substrate doping level when comparing b-Si emitters. Our simulation results also reveal that the predominant recombination mechanisms in the b-Si emitters were surface recombination and Auger recombination. Although the concentration of inactive P, which is one kind of SRH recombination center, is high in the nanofeature, the SRH recombination by such defects will be effectively suppressed due to the low concentration of minority carriers. Moreover, a small nanofeature will lead to less Auger recombination loss due to a small volume of the heavily-doped surface texture. The surface recombination velocity will be also lower as such a nanofeature will have a high surface dopant concentration and a deep dopant profile, which contribute to a low surface minority carrier density and the density at the tip can be even lower than $2\times10^{10}\ \text{cm}^{-3}$ at $5\times10^{16}\ \text{cm}^{-3}$ injection condition. As we have suggested that SSA is a more comprehensive metric than EAF for the comparison of different surface morphologies [26], we further prove that SSA is a good indicator of b-Si emitter electrical performance in this article. We conclude that a shallow nanotexture with $\text{SSA} > 100\ \mu\text{m}^{-1}$ and height < 100 nm should be chosen for R_{sheet} and J_{0e} optimization. However, to determine the best b-Si nanotexture design for the application of front-junction solar cells, the effects of SSA on the optical performance and the collection efficiency should also be investigated in future work.

ACKNOWLEDGMENT

The authors would like to thank the High Performance Computing service of Katana cluster by the Research Technology Services group at The University of New South Wales, like to thank the scientific and technical assistance of the Australian Microscopy and Microanalysis Research Facility at the Electron Microscope Unit, The University of New South Wales, like to thank M. Li at the University of Central Florida for the simulation suggestions, and also like to thank the RIE b-Si sample support by Rasmus Davidsen at the National Centre for Nanofabrication and Characterization, Technical University of Denmark. The responsibility for the views, information, or advice expressed herein is not accepted by the Australian Government.

REFERENCES

[1] X. Liu *et al.*, “Black silicon: Fabrication methods, properties and solar energy applications,” *Energy Environ. Sci.*, vol. 7, no. 10, pp. 3223–3263, 2014.

[2] M. Garin *et al.*, “Black-silicon ultraviolet photodiodes achieve external quantum efficiency above 130%,” *Phys. Rev. Lett.*, vol. 125, no. 11, 2020, Art. no. 117702.

[3] K. Oh *et al.*, “Black silicon photoanodes entirely prepared with abundant materials by low-cost wet methods,” *ACS Appl. Energy Mater.*, vol. 2, no. 2, pp. 1006–1010, 2019.

[4] X.-L. Liu *et al.*, ““Infinite sensitivity” of black silicon ammonia sensor achieved by optical and electric dual drives,” *ACS Appl. Mater. Interfaces*, vol. 10, no. 5, pp. 5061–5071, 2018.

[5] S. A. Iakab, P. Ràfols, M. Tajes, X. Correig-Blanchar, and M. García-Altares, “Gold nanoparticle-assisted black silicon substrates for mass spectrometry imaging applications,” *ACS Nano*, vol. 14, no. 6, pp. 6785–6794, 2020.

[6] F. Alexander *et al.*, “Water splitting TiO_2 composite material based on black silicon as an efficient photocatalyst,” *Sol. Energy Mater. Sol. Cells*, vol. 180, pp. 236–242, 2018.

[7] J. Oh, T. G. Deutsch, H.-C. Yuan, and H. M. Branz, “Nanoporous black silicon photocathode for H_2 production by photoelectrochemical water splitting,” *Energy Environ. Sci.*, vol. 4, no. 5, pp. 1690–1694, 2011.

[8] F. Yang *et al.*, “Dual protection layer strategy to increase photoelectrode–catalyst interfacial stability: A case study on black silicon photoelectrodes,” *Adv. Mater. Interfaces*, vol. 6, no. 8, 2019, Art. no. 1802085.

[9] Y. Yu *et al.*, “Enhanced photoelectrochemical efficiency and stability using a conformal TiO_2 film on a black silicon photoanode,” *Nature Energy*, vol. 2, no. 6, pp. 1–7, 2017.

[10] H. Savin *et al.*, “Black silicon solar cells with interdigitated back-contacts achieve 22.1% efficiency,” *Nature Nanotechnol.*, vol. 10, no. 7, pp. 624–628, 2015.

[11] P. Ortega *et al.*, "High-efficiency black silicon interdigitated back contacted solar cells on p-type and n-type c-Si substrates," *Prog. Photovolt., Res. Appl.*, vol. 23, no. 11, pp. 1448–1457, 2015.

[12] P. Ortega *et al.*, "Black silicon back-contact module with wide light acceptance angle," *Prog. Photovolt., Res. Appl.*, vol. 28, no. 3, pp. 210–216, 2020.

[13] G. Von Gastrow *et al.*, "Analysis of the atomic layer deposited Al_2O_3 field-effect passivation in black silicon," *Sol. Energy Mater. Sol. Cells*, vol. 142, pp. 29–33, 2015.

[14] P. Repo *et al.*, "Effective passivation of black silicon surfaces by atomic layer deposition," *IEEE J. Photovolt.*, vol. 3, no. 1, pp. 90–94, Jan. 2013.

[15] T. Rahman, R. S. Bonilla, A. Nawabjan, P. R. Wilshaw, and S. A. Boden, "Passivation of all-angle black surfaces for silicon solar cells," *Sol. Energy Mater. Sol. Cells*, vol. 160, pp. 444–453, 2017.

[16] W.-C. Wang *et al.*, "Surface passivation of efficient nanotextured black silicon solar cells using thermal atomic layer deposition," *ACS Appl. Mater. Interfaces*, vol. 5, no. 19, pp. 9752–9759, 2013.

[17] S. Wang *et al.*, "Field-effect passivation of undiffused black silicon surfaces," *IEEE J. Photovolt.*, vol. 11, no. 4, pp. 897–907, Jul. 2021.

[18] S. Wang *et al.*, "Understanding field-effect passivation of black silicon: Modeling charge carrier population control in compressed space charge regions," in *Proc. 47th IEEE Photovolt. Specialists Conf.*, 2020, pp. 0590–0594.

[19] J. Oh, H.-C. Yuan, and H. M. Branz, "An 18.2%-efficient black-silicon solar cell achieved through control of carrier recombination in nanostructures," *Nature Nanotechnol.*, vol. 7, no. 11, pp. 743–748, 2012.

[20] S. Zhong *et al.*, "High-efficiency nanostructured silicon solar cells on a large scale realized through the suppression of recombination channels," *Adv. Mater. Interfaces*, vol. 27, no. 3, pp. 555–561, 2015.

[21] H. Li *et al.*, "Influence of nanowires length on performance of crystalline silicon solar cell," *Appl. Phys. Lett.*, vol. 98, no. 15, 2011, Art. no. 151116.

[22] S. Zhong *et al.*, "Influence of the texturing structure on the properties of black silicon solar cell," *Sol. Energy Mater. Sol. Cells*, vol. 108, pp. 200–204, 2013.

[23] C. Wu *et al.*, "Forming submicron in micron texture on the diamond-wire-sawn mc-Si wafer by introducing artificial defects," *Prog. Photovolt., Res. Appl.*, vol. 28, no. 8, pp. 788–797, 2020.

[24] K. Chen *et al.*, "MACE nano-texture process applicable for both single-and multi-crystalline diamond-wire sawn Si solar cells," *Sol. Energy Mater. Sol. Cells*, vol. 191, pp. 1–8, 2019.

[25] F. Cao *et al.*, "Next-generation multi-crystalline silicon solar cells: Diamond-wire sawing, nano-texture and high efficiency," *Sol. Energy Mater. Sol. Cells*, vol. 141, pp. 132–138, 2015.

[26] G. Scardera *et al.*, "On the enhanced phosphorus doping of nanotextured black silicon," *IEEE J. Photovolt.*, vol. 11, no. 2, pp. 298–305, Mar. 2021.

[27] *Sentaurus Process User Guide*, vol. L-2016.03. Mountain View, CA, USA: Synopsys, 2016.

[28] *Sentaurus Device User Guide*, vol. L-2016.03. Mountain View, CA, USA: Synopsys Inc., 2016.

[29] A. Schenk, "Finite-temperature full random-phase approximation model of band gap narrowing for silicon device simulation," *J. Appl. Phys.*, vol. 84, no. 7, pp. 3684–3695, 1998.

[30] D. Klaassen, "A unified mobility model for device simulation—I. Model equations and concentration dependence," *Solid-State Electron.*, vol. 35, no. 7, pp. 953–959, 1992.

[31] J. Schön *et al.*, "Predictive simulation of doping processes for silicon solar cells," *Energy Procedia*, vol. 38, pp. 312–320, 2013.

[32] H. Mäckel and K. Varner, "On the determination of the emitter saturation current density from lifetime measurements of silicon devices," *Prog. Photovolt., Res. Appl.*, vol. 21, no. 5, pp. 850–866, 2013.

[33] A. Richter, S. W. Glunz, F. Werner, J. Schmidt, and A. Cuevas, "Improved quantitative description of auger recombination in crystalline silicon," *Phys. Rev. B*, vol. 86, no. 16, 2012, Art. no. 165202.

[34] B. Min *et al.*, "Heavily doped Si:P emitters of crystalline Si solar cells: Recombination due to phosphorus precipitation," *Physica Status Solidi –Rapid Res. Lett.*, vol. 8, no. 8, pp. 680–684, 2014.

[35] K. R. McIntosh and L. E. Black, "On effective surface recombination parameters," *J. Appl. Phys.*, vol. 116, no. 1, 2014, Art. no. 014503.

[36] P. P. Altermatt *et al.*, "Numerical modeling of highly doped Si:P emitters based on Fermi–Dirac statistics and self-consistent material parameters," *J. Appl. Phys.*, vol. 92, no. 6, pp. 3187–3197, 2002.

[37] P. Li *et al.*, "Effective optimization of emitters and surface passivation for nanostructured silicon solar cells," *RSC Adv.*, vol. 6, no. 106, pp. 104073–104081, 2016.

[38] K. R. McIntosh and L. P. Johnson, "Recombination at textured silicon surfaces passivated with silicon dioxide," *J. Appl. Phys.*, vol. 105, no. 12, 2009, Art. no. 124520.

[39] A. Cuevas *et al.*, "Carrier population control and surface passivation in solar cells," *Sol. Energy Mater. Sol. Cells*, vol. 184, pp. 38–47, 2018.

[40] T. H. Fung *et al.*, "Improved emitter performance of RIE black silicon through the application of in-situ oxidation during $POCl_3$ diffusion," *Sol. Energy Mater. Sol. Cells*, vol. 210, 2020, Art. no. 110480.

[41] T. Pasanen, V. Vähänissi, N. Theut, and H. Savin, "Surface passivation of black silicon phosphorus emitters with atomic layer deposited SiO_2/Al_2O_3 stacks," *Energy Procedia*, vol. 124, pp. 307–312, 2017.

[42] P. Zhang *et al.*, "The influence of Ag-Ion concentration on the performance of mc-Si silicon solar cells textured by metal assisted chemical etching (MACE) method," *Sol. Energy Mater. Sol. Cells*, vol. 200, 2019, Art. no. 109983.

[43] P. Li *et al.*, "Highly efficient industrial large-area black silicon solar cells achieved by surface nanostructured modification," *Appl. Surf. Sci.*, vol. 357, pp. 1830–1835, 2015.

[44] Y. Zhuang, S. Zhong, Z. Huang, and W. Shen, "Versatile strategies for improving the performance of diamond wire sawn mc-Si solar cells," *Sol. Energy Mater. Sol. Cells*, vol. 153, pp. 18–24, 2016.

[45] I. R. Putra, J.-Y. Li, and C.-Y. Chen, "18.78% hierarchical black silicon solar cells achieved with the balance of light-trapping and interfacial contact," *Appl. Surf. Sci.*, vol. 478, pp. 725–732, 2019.